Experimental observation of the stratified electrothermal instability on aluminum with thickness greater than a skin depth

T. M. Hutchinson,[1,*] T. J. Awe,[2] B. S. Bauer,[1] K. C. Yates,[3] E. P. Yu,[2] W. G. Yelton,[2] and S. Fuelling[1]
[1]*University of Nevada, Reno, Nevada 89506, USA*
[2]*Sandia National Laboratories, Albuquerque, New Mexico 87185, USA*
[3]*University of New Mexico, Albuquerque, New Mexico 87131, USA*

(Received 24 July 2017; revised manuscript received 26 January 2018; published 17 May 2018)

A direct observation of the stratified electrothermal instability on the surface of thick metal is reported. Aluminum rods coated with 70 μm Parylene-N were driven to 1 MA in 100 ns, with the metal thicker than the skin depth. The dielectric coating suppressed plasma formation, enabling persistent observation of discrete azimuthally correlated stratified thermal perturbations perpendicular to the current whose wave numbers, k, grew exponentially with rate $\gamma(k) = 0.06\,\mathrm{ns}^{-1} - (0.4\,\mathrm{ns}^{-1}\,\mu\mathrm{m}^2\,\mathrm{rad}^{-2})\,k^2$ in $\sim$1 g/cm^3, $\sim$7000 K aluminum.

DOI: 10.1103/PhysRevE.97.053208

I. INTRODUCTION

Understanding the evolution of a conductor carrying intense current requires knowledge of its instabilities. One important mode that can grow exponentially is the electrothermal instability (ETI): a reinforcement of temperature perturbations by the nonuniform ohmic heating they cause. Prediction of the course of this primordial instability is needed to obtain the initial amplitude and spectrum of perturbations that seed subsequent magnetohydrodynamic (MHD) instabilities [1,2]. Understanding this seeding is vital for developing off-Hugoniot equation of state measurements [3], magnetically insulated transmission lines [4,5], magnetically accelerated flyer plates [6], and magnetoinertial fusion [7–9] devices.

While the ETI has been discussed theoretically for over half a century [10], direct observation has been missing for a large, important class of common situations, including the applications above. In metal, the ETI produces alternating high and low temperature bands (strata, δT) perpendicular to the current. However, this growth has only been observed when the electrical skin depth is larger than the conductor's smallest cross sectional dimension (the thin-wire regime) [11–20]. When this inequality is reversed (i.e., the *thick* regime) and the skin layer ohmically heats, the rising current shunts [21–25] to underlying cold, conductive layers, and therefore the instability drive at the surface is strongly diminished [26]. This effectively adds a new dimension to the physics of the surface evolution and the ETI. For example, numerical solutions to the linearized ETI equations that include nonlinear magnetic diffusion, but not hydrodynamics, indicate negligible ETI growth on the outer surface of a current-carrying metal tube [25]. However, 2D [27–30] and full 3D [26] resistive MHD simulations in the thick-rod regime demonstrate ETI growth when the conductor is still in the solid phase and show significant temperature and density modulations (δT and $\delta\rho$) after the surface vaporizes. In addition, the existence and influence of the ETI has been inferred in thick-regime experiments, but ETI growth has not been directly observed [27,29,31]. Since the $\delta\rho$ produced by the ETI are challenging to distinguish from those amplified by the magneto-Rayleigh-Taylor instability, explicit identification of the ETI requires measurement of δT. However, emissions from ETI strata are easily overwhelmed by emissions from nonuniform plasmas or non-MHD processes typical of many load-hardware configurations [32–35].

This article reports the first direct observation of the stratified electrothermal instability on the surface of thick metal. The nonlinear growth of strata was captured in a series of high resolution (3 μm), time-gated (2–13 ns) images of surface emissions. In addition, the dielectric coating suppresses surface plasma that forms on uncoated rods, therefore surface strata are observable for much longer [32–35]. Facilitated by this longevity, measurements of the ETI dispersion relation represent a new way to constrain transport properties in warm dense matter, an increasingly important field in which consensus between vastly different model predictions of thermal and electrical conductivities is hampered by the scarcity of measurements [36–44].

II. EXPERIMENTAL SETUP

Thick-rod experiments were performed using the 1-MA, 100-ns Zebra generator [45,46], with compressed knife-edge anode-cathode coupling hardware that mitigates nonthermal plasma formation [32,34]. Rod surfaces were carefully characterized to identify initial perturbations from which the ETI may grow. Aluminum 6061 was machined on a lathe and surfaces were electrochemically smoothed to produce 11 rods with diameter 974 ± 9 μm and average absolute surface displacement $\delta_a = 220 \pm 40$ nm. The polymer Parylene-N [poly(p-xylylene) $(C_8H_8)_n$], a transparent dielectric [47,48], was chemical vapor deposited around 5 aluminum rods to thickness 70 ± 5 μm. Aluminum surface characterization (Fig. 1) included white light interferometry (WLI), scanning electron microscopy (SEM), and energy dispersive x-ray

*trevorhutchinson@unr.edu

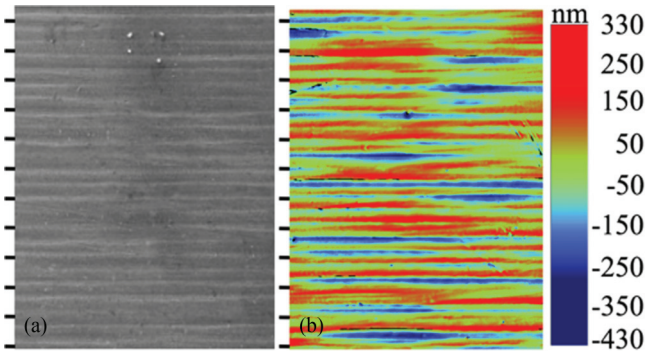

FIG. 1. Preshot topographical characterization of aluminum rod surfaces after electropolishing and before coating. (a) 10 kV SEM (secondary electron) image of an aluminum rod surface, 94 μm × 125 μm. The figure's horizontal dimension is azimuthal in the experiment, and the vertical dimension is parallel to the rod axis ($\hat{z}$) and the electric current density $\boldsymbol{j}$. (b) WLI image of aluminum rod surface, with the same orientation as in (a), 94 μm × 125 μm. Color signifies surface displacement in nanometers in the ± radial direction. Tick marks are separated by 10 μm. Surface structure in (a), (b) was consistent across the 11 rods, although (a) and (b) are not of the same surface.

spectroscopy (EDS). Some discrete, embedded, and resistive surface imperfections [inclusions, Fig. 1(a)] remained after electropolishing. These were determined by EDS to be principally composed of the alloying elements (silicon and magnesium) specific to aluminum 6061.

A suite of diagnostics examined rod surfaces with high spatial and temporal resolution. Emissions from surface aluminum were imaged, with magnification $M = 22$, onto two independently gated, intensified-charge-coupled devices (ICCD), using a Questar QM-100 long distance microscope and a 28-mm-focal-length Nikkor lens. ICCD camera 1 (C1) was an Andor DH334T-18U-73 while camera 2 (C2) was an Andor DH734-18F-A3. In addition, unfiltered, visible emissions from load surfaces were imaged onto a photodiode array (PDA) to measure the full time-evolution of emissions, with coarse axial resolution. Finally, two laser shadowgraphs (separated by 15 ns) were captured on each discharge using a 532-nm-wavelength, 150-ps, 100-mJ pulsed Ekspla laser. Shadowgraphs were used to characterize load expansion and to evaluate macroscopic late-time surface instability amplitudes.

III. DATA AND ANALYSIS

ICCD imaging (Fig. 2) shows that discrete strata (perpendicular to the electric current density, $\boldsymbol{j}$) form on the surface of ohmically heated thick aluminum, and that filaments (parallel to $\boldsymbol{j}$) do not form on dielectric coated loads as late as 140 ns. Theory predicts that for material with electrical resistivity (η) rising with temperature ($\partial\eta/\partial T > 0$), the fastest-growing ETI mode is a banded/stratified temperature perturbation with strata perpendicular to $\boldsymbol{j}$. When plasma forms and $\partial\eta/\partial T < 0$, the instability manifests filamentary δT parallel to $\boldsymbol{j}$—therefore, the absence of filaments suggests plasma does not form on dielectric or aluminum surfaces of coated-rods [10,17,19]. Coated loads [Figs. 2(a)–2(d)] first display structured emissions from strata up to 200 μm in azimuthal extent. On average, however, strata are azimuthally contained within 70 ± 20 μm in Fig. 2(a), and within 40 ± 20 μm in Fig. 2(d),

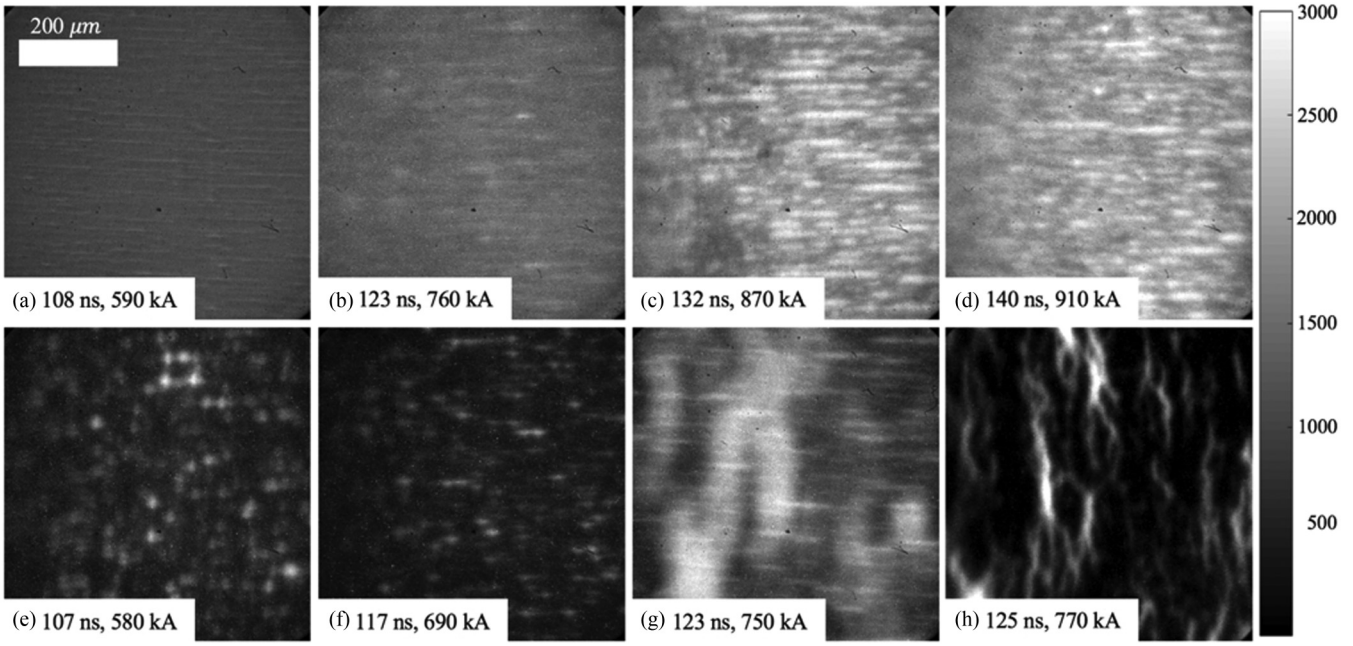

FIG. 2. ICCD time-gated images of structured emissions from current-carrying 1-mm-diameter aluminum 6061 surfaces (614 μm × 614 μm for each full image, or see scale bar in [a]), coated with 70 μm Parylene-N (top row) and uncoated (bottom row). The vertical dimension ($\hat{z}$) is nearly parallel to $\boldsymbol{j}$ (to within ± 2°, corrected during analysis), and the gray-scale bar denotes (background-subtracted) counts per nanosecond. Frame (h) was taken by C1, and the remainder by C2. Frame times correspond to halfway through the ICCD microchannel plate voltage pulse for that frame (the midframe time, MFT). There is a ±3 ns uncertainty in ICCD timing.

interestingly consistent with [26] despite the difference in metallic composition. Interstrata axial distances and intrastrata axial full width at half maxima grow with increasing load current. Relative to emissions from background aluminum, emissions from strata in Figs. 2(a)–2(d) increase nonlinearly by over an order of magnitude. An analysis of strata growth across the ICCD images of coated loads is given after theoretical predictions, below.

An understanding of coated loads benefits from an understanding of the evolution of bare aluminum, where ICCD and SEM evidence show strata forming via nonuniform heating of resistive perturbations [inclusions, Fig. 1(a)] [34]. "Spots" on uncoated loads azimuthally stretch with increasing load current [Figs. 2(e)–2(g)], forming up to 100-μm-wide strata [34]. After ≈5 ns, filaments form [Figs. 2(g) and 2(h)] and rapidly outshine strata. In addition, MHD modeling of untamped aluminum shows that plasma forms in low-density resistive metallic vapor because ohmic heating exceeds the combined rates of cooling by expansion, radiation, and thermal conduction [35]. Finally, filaments often connect spots/strata at the same azimuthal location [Figs. 2(g) and 2(h)], indicating spots/strata explode before or faster than ambient aluminum.

The Parylene-N coating remained sufficiently transparent for the strata on the metal to be observed during the 100-ns current rise time. Because Parylene-N is 10^{23} times more resistive than aluminum, current is expected to flow almost entirely in the aluminum [49,50]. The stratified ETI is not expected to grow in dielectrics [29,31], so observable strata confirm that the current flows in the aluminum. Since Parylene-N has a bulk dielectric strength (235 MV/m) [51] approximately one hundred times greater than the maximum electric field in the experiment (2.1–2.4 MV/m, calculated via circuit modeling and MHD simulations [35]), bulk dielectric breakdown is not expected. The diffusion of heat radially outwards into the Parylene-N has a skin depth of $\sqrt{2\kappa t/c_v\rho} \approx 500$ nm [49] (where c_v is specific heat, and κ thermal conductivity) on the 100-ns experimental timescale. This means only a thin dielectric layer is appreciably heated by thermal transport from aluminum. Similarly, in the extreme hypothetical case that all the energy radiated in 100 ns from optically thick aluminum at $T = 8700$ K (using the Stefan-Boltzmann Law) were fully absorbed [47,48] in the closest 1 μm of Parylene-N, this volume would only be heated from room temperature by ≈23 K. These calculations, and that strata appear in imaging, support that the bulk of the dielectric remains transparent throughout the experiment.

Shadowgraphs show that the Parylene-N coating tamps the aluminum explosion. Coated rod diameters (including the dielectric coating), although initially 140 μm larger in diameter, are less than those of uncoated rods during observation of the ETI (Fig. 3), demonstrating tamping. Illumination light is scattered out of the beam path by the dielectric coating, so shadowgraphy does not directly measure the aluminum expansion in coated loads. In addition, uncoated loads have been demonstrated to expand linearly until near peak current [52]; therefore, extrapolation of uncoated rod data in Fig. 3 indicates an electrical explosion of surface aluminum occurs at 70 ns (which should also apply for coated loads). Finally, uncoated aluminum shadowgraphs show MHD instabilities of

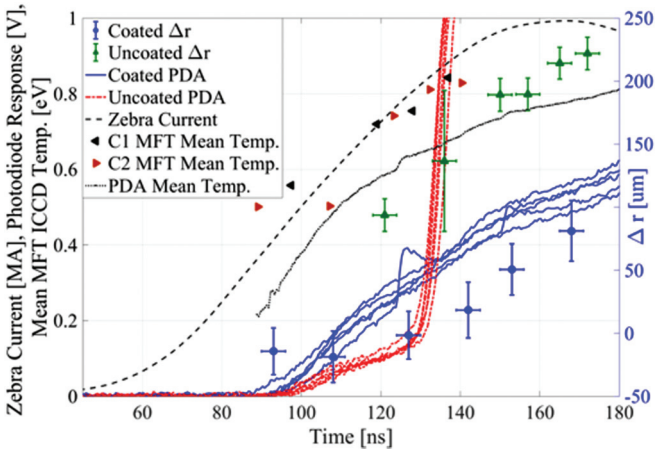

FIG. 3. Time-resolved visible emissions from, and change in radii (Δr) of, coated and uncoated, current-carrying 1-mm-diameter aluminum-6061 rods. A representative Zebra current waveform is shown. All times are synchronized to a common time axis where 500 kA occurs at 100 ns. Rods used to provide Δr data (upward, green triangles) were single-point diamond turned and have ultralow surface roughness ($\delta_a = 42$ nm) but are otherwise identical to uncoated rods. Variation of macroscopic $\Delta r(t)$ with surface roughness has not been observed [52], justifying surrogacy of these measurements for uncoated-rod diameters. Vertical error bars correspond to 10%–90% edge-response and horizontal to shadowgraph timing uncertainty. Also plotted is the average of four regions of interest (ROI) [55] temperatures (estimated by radiometry) for each coated load image from ICCD C1 (◁) and C2 (▷) vs mid-frame time (MFT), along with the $\langle T_{BB}\rangle$ calculated from PDA radiometry (dotted black line, averaged over the 5 coated-load PDA traces). Mean temperatures are only plotted for $t > 89$ ns, when the signals exceed the noise.

amplitude ≈50 μm (consistent with [52]), while coated-rod shadowgraphs do not display surface perturbations to within the diagnostic resolution of 19 μm, suggesting an absence of plasma on the outside of the Parylene-N.

The evolution of surface emissions (measured by PDA) further supports that Parylene-N tamps aluminum expansion and suppresses plasma formation. Before 130 ns, the average ratio of spatially integrated emissions from coated loads to those from uncoated loads (Fig. 3) is a nearly constant 2.3 ± 0.1. This is partly the result of greater pdV cooling of untamped (relative to tamped) aluminum by a factor proportional to the ratio of the aluminum expansion velocities of the two load types. At 130 ns, uncoated loads abruptly brighten; this rapid increase in visible emissions is correlated with plasma formation [33,52] and concurrent with ICCD images displaying a transition to filamentary structures [see Figs. 2(g) and 2(h)] or Fig. 1 of Ref. [34]), which theory suggests will develop as plasma forms. Consequently, the absence of this sharp rise in emissions from coated loads is an indication plasma does not form on their dielectric surface. Indeed, tamping of expanding metal and plasma suppression by dielectric coating are also seen in the thin-wire regime [53].

To calculate the spectral evolution and growth rate of the ETI modes observed in the ICCD images, the measured emissions were first mapped to temperature estimates. By assuming exploding aluminum ($T > 2750$ K, the boiling point [50])

emits as a blackbody, and considering the spectral response of every element in each camera's optical path, the number of counts at each pixel was converted to a lower-bound blackbody surface temperature (T_{BB}) estimate. Similarly, an average blackbody surface temperature ($\langle T_{BB}\rangle$) was also calculated from PDA signals. ICCD and PDA data together indicate an average surface temperature 3,000–10,000 K during the growth of the ETI (Fig. 3).

While the complete, tamped, hydrodynamic case has not been addressed by theory, it is useful to estimate the ETI growth rate via thick-rod MHD simulations. For example, 2D [27] and 3D [26] MHD calculations suggest the temperature growth rate of the ETI in uncoated thick aluminum rods carrying $j_1 \approx 2$ MA/mm^2 is $\gamma_1 \approx 0.1$ ns^{-1}. However, Ref. [29] suggests that, under the same conditions, a 50-μm-thick dielectric coating diminishes γ_1 severalfold. However, while the ETI is observed on Zebra (500–900 kA), theory and simulations [23,27,30] suggest a smaller $j_2 \approx 1$ MA/mm^2 in the nonlinear current-density wave propagating into the aluminum, which is only half j_1 in simulations [26] and [27]. This would indicate that the experimentally observed growth rate should be less than $\gamma_1 \approx 0.1$ ns^{-1}.

In contrast, hydrodynamic-free, thin-wire ETI theory suggests relatively slow growth rates for this experiment. Excluding hydrodynamics, which shuts off the ETI $\delta\rho$ feedback mechanism, the ETI exponential growth rate of δT, derived by perturbing the thermal energy balance equation [19], is

$$\gamma = \frac{\frac{\partial \eta}{\partial T} j^2 - \kappa k_z^2}{c_v \rho}. \tag{1}$$

In the long wavelength limit (mode wavenumber $k_z \to 0$), Eq. (1) yields a maximum ETI growth rate $\gamma_2(\rho_s) \approx 0.01$ ns^{-1}, using illustrative estimated parameters j_2, $\rho_s = 2.7$ g/cm^3, $c_v = 927$ J/(kg K), and $\partial\eta/\partial T = 2.3 \times 10^{-11}$ Ω m/K (from the Lee-Moore-Desjarlais (LMD) Sesame 29373 table for the 3500–8000 K range [54]).

A lower bound on the aluminum density may be inferred from the fact that filaments do not appear in ICCD images of coated loads. The absence of filaments suggests <8 filamentation instability growth times have elapsed before each frame. Using $\langle T_{BB}\rangle$ and the LMD table, a calculation of the maximum filamentation growth rate [11] as a function of density suggests the tamped aluminum density is at least $\rho_{min} = 0.63$ g/cm^3.

Fourier analysis of ICCD T_{BB} maps of coated loads show strata evolution is wavelength dependent. After the surface has exploded, when the current is around 300 kA, no structure is evident in the spectra. The earliest appearing perturbations [at ~500 kA, seen in Fig. 2(a)] have axial wavelength contributions that match those of the machining structure (modes of wavelength $\lambda < 20$ μm). Over the next 30 ns (~500 to ~800 kA), modes with $\lambda > 15$ μm (axial wave number $k_z < 0.4$ rad/μm) grow exponentially, while short-wavelength ($\lambda < 15$ μm) modes matching machining structure decay. Finally, long-wavelength modes grow to a maximum amplitude by ~800 kA. From the standpoint of linear instability theory, this indicates that the dominant, 5 μm [via Fourier analysis of Fig. 1(b)] machining structure is not directly responsible for the late-time strata. These later strata [Figs. 2(c) and 2(d)] may be generated by the nonlinear evolution of inclusions, or by machining perturbations with axial wavelength >15 μm.

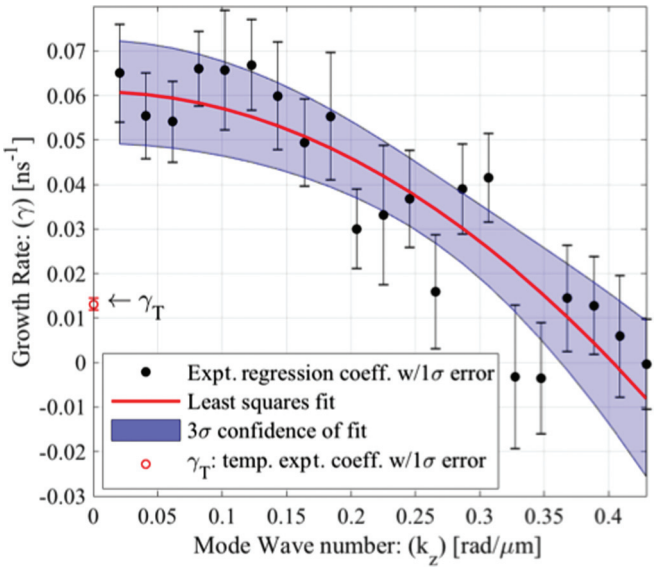

FIG. 4. Exponential growth rates, γ (ns^{-1}), fit from Fourier amplitudes vs. time, for small-wave number (k_z [rad/μm]) modes in temperature maps from ICCD images, from 500–800 kA (this range excludes the earliest and latest pairs of ICCD images, where growth is not observed). Fourier coefficients are calculated from azimuthally-averaged (57 μm), axial lineouts of temperature-mapped ICCD images [55]. The red dispersion curve represents the least squares fit to $\gamma(k_z) = \gamma_{max} - mk_z^2$ [Eq. (1)], and the blue region a $\pm 3\sigma$ confidence band of this fit [56]. The red circle at $k_z = 0$ denotes an effective growth rate, $\gamma_T = 0.014$ ns^{-1}, from the exponential fit of the mean ICCD temperatures from Fig. 3. Growth rates with wavenumber greater than $k_z \sim 0.45$ rad/μm are γ_T to within experimental error.

An ETI dispersion curve (Fig. 4) relating growth rate γ to wavenumber k_z was obtained by computing linear regressions of the logarithms of Fourier mode amplitudes vs time, during the period of exponential growth (98–132 ns). Modes with small wavenumber ($k_z < 0.2$ rad/μm) grow at a rate much bigger than the effective exponential growth rate of the average temperature, γ_T, over the same time period. This indicates the presence of an electrically driven thermal instability in the thick-rod regime–that is, the presence of a feedback mechanism active in surface aluminum layers by which hotter regions (strata) receive more joule heating than cooler ones. In addition, the growth rates fit well to the theoretically motivated parabola (e.g., Eq. (1) above and Eq. (28) of Ref. [19]) $\gamma(k_z) = \gamma_{max} - mk_z^2$, with $\gamma_{max} = 0.061 \pm 0.004$ ns^{-1} and $m = 0.37 \pm 0.04$ ns^{-1} μm^2 rad^{-2}. Using Eq. (1), the quadratic coefficient, m, is related to the thermal conductivity of exploded aluminum as $\kappa_{exp} = mc_v\rho$. Using sample parameters $c_v = 927$ J/(kg K) and $\rho = 1$ g/cm^3, we coarsely estimate $\kappa_{exp} \sim 300$ W/(m K), while Sesame 29373 suggests $\kappa_{ses} \sim 100$ W/(m K) for $\rho = 1$ g/cm^3 and $T = 1$ eV. These order-of-magnitude agreements between theory and experiment (of γ and κ) indicates that the ETI can act as a diagnostic of warm dense matter. With detailed modeling and refined experiments, accuracy of κ_{exp} will likely improve, assisting in the discrimination between

available models of the ETI and the transport properties of warm dense matter.

IV. CONCLUSION

In conclusion, ETI strata were observed on the aluminum surface of thick rods with and without a 70 μm Parylene-N coating. Axial temperature perturbations grow exponentially with rates up to $\gamma_{max} = 0.06$ ns^{-1} on dielectric-coated aluminum surfaces. Laser shadowgraphs and time-resolved visible emissions (measured by PDA) indicate the dielectric coating hydrodynamically tamps expanding aluminum. ICCD images, time-resolved visible emissions, and shadowgraphs indicate dielectric coatings suppress plasma formation. Since strata only appear for $\sim$5 ns on uncoated loads, but exist for $>$30 ns on coated loads, we have demonstrated the viability of a novel platform for investigating ETI evolution, paving the way for more systematic studies of this difficult-to-diagnose phenomenon and of warm dense matter.

ACKNOWLEDGMENTS

The authors would like to thank R. Bauer, D. Cliche, W. Cline, E. Dutra, G. Grossetete, S. Hansen, V. Ivanov, J. Jarrell, J. Kaushagen, B. McKenzie, J. Mei, J. Paul, J. Pillars, and the Zebra staff for useful conversations and/or technical assistance. We would also like to thank K. Cochrane for access to and assistance with Sesame tables. T.H. would like to thank Sandia management and R. McBride for their support. B.B. was in part supported by sabbatical assistance from the University of Nevada, Reno. This work was funded in part by Sandia's Laboratory Directed Research and Development Program (Projects No. 178661 and No. 200269). Sandia National Laboratories is a multi-mission laboratory managed and operated by National Technology and Engineering Solutions of Sandia, LLC., a wholly owned subsidiary of Honeywell International, Inc., for the U.S. Department of Energy's National Nuclear Security Administration under Contract No. DE-NA-0003525.

[1] D. B Sinars, S. A. Slutz, M. C. Herrmann, R. D. McBride, M. E. Cuneo, K. J. Peterson, R. A. Vesey, C. Nakhleh, B. E. Blue, K. Killebrew *et al.*, Phys. Rev. Lett. **105**, 185001 (2010).

[2] R. D. McBride, S. A. Slutz, C. A. Jennings, D. B. Sinars, M. E. Cuneo, M. C. Herrmann, R. W. Lemke, M. R. Martin, R. A. Vesey, K. J. Peterson *et al.*, Phys. Rev. Lett. **109**, 135004 (2012).

[3] M. R. Martin, R. W. Lemke, R. D. McBride, J. P. Davis, D. H. Dolan, M. D. Knudson, K. R. Cochrane, D. B. Sinars, I. C. Smith, M. Savage *et al.*, Phys. Plasmas **19**, 056310 (2012).

[4] W. A. Stygar, P. A. Corcoran, H. C. Ives, R. B. Spielman, J. W. Douglas, B. A. Whitney, M. A. Mostrom, T. C. Wagoner, C. S. Speas, T. L. Gilliland *et al.*, Phys. Rev. Special Topics—Accelerat. Beams **12**, 120401 (2009).

[5] W. A. Stygar *et al.*, Phys. Rev. Special Topics—Accelerat. Beams **18**, 110401 (2015).

[6] R. W. Lemke, M. D. Knudson, K. R. Cochrane, M. P. Desjarlais, and J. R. Asay, J. Physics Conf. Series **500**, 152009 (2014).

[7] S. A. Slutz, M. C. Herrmann, R. A. Vesey, A. B. Sefkow, D. B. Sinars, D. C. Rovang, K. J. Peterson, and M. E. Cuneo, Phys. Plasmas **17**, 056303 (2010).

[8] M. R. Gomez, S. A. Slutz, A. B. Sefkow, K. D. Hahn, S. B. Hansen, P. F. Knapp, P. F. Schmit, C. L. Ruiz, D. B. Sinars, E. C. Harding *et al.*, Phys. Plasmas **22**, 056306 (2015).

[9] G. A. Wurden, S. C. Hsu, T. P. Intrator, T. C. Grabowski, J. H. Degnan, M. Domonkos, P. J. Turchi, E. M. Campell, D. B. Sinars, M. C. Hermann, R. Betti, B. S. Bauer, I. R. Lindemuth, R. E. Siemon, R. L. Miller, M. Laberge, and M. Delage, J. Fusion Energy **35**, 69 (2016).

[10] B. B. Kadomtsev, *Reviews of Plasma Physics*, Vol. 2, edited by M. A. Leontovich (Plenum, New York, 1966), p.195.

[11] R. B. Baksht, A. G. Rousskikh, A. S. Zhigalin, V. I. Oreshkin, and A. P Artyomov, Phys. Plasmas **22**, 103521 (2015).

[12] D. B Sinars, T. A. Shelkovenko, S. A. Pikuz, J. B. Greenly, and D. A. Hammer, Phys. Plasmas **7**, 1555 (2000).

[13] A. G. Rousskikh, V. I. Oreshkin, S. A. Chaikovsky, N. A. Labetskaya, A. V. Shishlov, I. I Beilis, and R. B. Baksht, Phys. Plasmas **15**, 102706 (2008).

[14] R. B. Baksht, S. I. Tkachenko, V. M. Romanova, A. R. Mingaleev, V. I. Oreshkin, A. E. Ter-Oganes'yan, T. A. Khattatov, T. A. Shelkovenko, and S. A. Pikuz, Tech. Phys. **58**, 1129 (2013).

[15] L. Atoyan, T. Byvank, A. D. Cahill, C. L. Hoyt, P. W. L. de Grouchy, W. M. Potter, B. R. Kusse, and D. A. Hammer, AIP Conf. Proc. **1639**, 67 (2014).

[16] A. S. Zhigalin, A. G. Rousskikh, V. I. Oreshkin, S. A. Chaikovsky, N. A. Ratakhin, K. V. Khishchenko, and R. B. Baksht, J. Phys: Conf. Series **653**, 012146 (2015).

[17] D. D. Ryutov, M. S. Derzon, and M. K. Matzen, Rev. Mod. Phys. **72**, 167 (2000).

[18] Y. U. Raizer. *Gas Discharge Physics* (Springer, Berlin, 1991), Sec. 9.4.

[19] V. I. Oreshkin, Phys. Plasmas **15**, 092103 (2008).

[20] V. I. Oreshkin, R. B. Baksht, N. A. Ratakhin, A. V. Shishlov, K. V. Khishchenko, P. R. Levashov, and I. I Beilis, Phys. Plasmas **11**, 4771 (2004).

[21] S. A. Chaikovsky, V. I. Oreshkin, I. M Datsko, N. A. Labetskaya, D. V. Rybka, and N. A. Ratakhin, Phys. Plasmas **22**, 112704 (2015).

[22] N. A. Labetskaya, V. I. Oreshkin, S. A. Chaikovsky, I. M. Datsko, N. I. Kuskova, and A. D. Rud, J. Phys: Conf. Series **552**, 012020 (2014).

[23] O. Schnitzer, Phys. Plasmas **21**, 082306 (2015).

[24] H. E. Knoepfel, *Magnetic Fields: A Comprehensive Theoretical Treatise for Practical Use* (Wiley, New York, 2000), Sec. 5.4.

[25] V. I. Oreshkin and S. A. Chaikovsky, Phys Plasmas **19**, 022706 (2012).

[26] J. D. Pecover and J. P Chittenden, Phys. Plasmas **22**, 102701 (2015).

[27] K. J. Peterson, D. B. Sinars, E. P. Yu, M. C. Herrmann, M. E. Cuneo, S. A. Slutz, I. C. Smith, B. W. Atherton, M. D. Knudson, and C. Nakhleh, Phys. Plasmas **19**, 092701 (2012).

[28] K. J. Peterson, E. P. Yu, D. B. Sinars, M. E. Cuneo, S. A. Slutz, J. M. Koning, M. M. Marinak, C. Nakhleh, and M. C. Herrmann, Phys. Plasmas **20**, 056305 (2013).

[29] K. J. Peterson, T. J. Awe, E. P. Yu, D. B. Sinars, E. S. Field, M. E. Cuneo, M. C. Hermann, M. Savage, D. Schroen, K. Tomlinson *et al.*, Phys. Rev. Lett. **112**, 135002 (2014).

[30] V. I. Oreshkin, S. A. Chaikovsky, I. M. Datsko, N. A. Labetskaya, G. A. Mesyats, E. V. Oreshkin, N. A. Ratakhin, and D. V. Rybka, Phys. Plasmas **23**, 122107 (2016).

[31] T. J. Awe, K. J. Peterson, E. P. Yu, R. D. McBride, D. B. Sinars. M. R. Gomez, C. A. Jennings, M. R. Martin, S. E. Rosenthal, D. G. Schroen *et al.*, Phys. Rev. Lett. **116**, 065001 (2016).

[32] T. J. Awe, B. S. Bauer, S. Fuelling, and R. E. Siemon, Phys. Plasmas **18**, 056304 (2011).

[33] T. J. Awe, B. S. Bauer, S. Fuelling, and R. E. Siemon, Phys. Rev. Lett. **104**, 035001 (2010).

[34] T. J. Awe, E. P. Yu, K. C. Yates, W. G. Yelton, B. S. Bauer, T. M. Hutchinson, S. Fuelling, and B. B. McKenzie, IEEE Trans. Plasma Sci. **45**, 584 (2017).

[35] I. R. Lindemuth, R. E. Siemon, B. S. Bauer, M. A. Angelova, and W. L. Atchison, Phys. Rev. Lett. **105**, 195004 (2010).

[36] S. X. Hu, L. A. Collins, T. R. Boehly, J. D. Kress, V. N. Goncharov, and S. Skupsky, Phys. Rev. E **89**, 043105 (2014).

[37] T. Takahashi, Y. Kawaguchi, T. Ohuchi, K. Takahashi, T Sasaki, T. Kikuchi, T Aso, and N. Harada, J. Phys. Conf. Ser. **688**, 012100 (2016).

[38] S. Sugimoto, A. Watabe, Y. Sugimoto, S. Kusano, K. Takahashi, T. Kikuchi, and N. Harada, Phys. Plasmas **24**, 072703 (2017).

[39] J. F. Benage, Phys. Plasmas **7**, 2040 (2000).

[40] A. W. DeSilva and A. D. Rakhel, Contrib. Plasma Phys. **45**, 236 (2005).

[41] Y. Amano, Y. Miki, T. Takahashi, T. Sasaki, T. Kikichi, and N. Harada, Rev. Sci. Ins. **83**, 085107 (2012).

[42] T. Sasaki, Y. Yano, M. Nakajima, T. Kawamura, and K. Horioka, Las. Part. Beams **24**, 371 (2006).

[43] F. Graziani, M. P. Desjarlais, R. Redmer, and S. B. Trickey, eds., *Frontiers and Challenges in Warm Dense Matter* (Springer, Berlin, 2014).

[44] A. McKelvey, G. E. Kemp, P. A. Sterne, A. Fernandez-Panella, R. Shepherd, M. Marinak, A. Link. G. W. Collins, H. Sio, J. King, R. R. Freeman, R. Hua, C. McGuffey, J. Kim, F. N. Beg, and Y. Ping, Nat. Sci. Rep. **7**, 7015 (2017).

[45] B. S. Bauer, V. L. Kantsyrev, N. Le Galloudec, R. Presura, G. S. Sarkisov, A. S. Shlyaptseva, S. Batie, W. Brinsmead, H. Faretto, B. Le Galloudec *et al.*, *Proceedings of the 12th International Pulsed Power Conference*, Vol. 2 (IEEE, Monterey, CA, 1999), p. 1045.

[46] B. S. Bauer, V. L. Kantsyrev, F. Winterberg, A. S. Shylaptseva, R. C. Mancini, H. Li, and A. Oxner, *Proceedings of the 4th International Conference on Dense Z-Pinches*, edited by N. R. Pereira *et al.* (AIP, College Park, MD, 1997).

[47] Y. S. Jeong, B. Ratier, A. Moliton, and L. Guyard, Synth. Metals **127**, 189 (2002).

[48] R. Machorro, L. E. Regalado, and J. M. Siqueiros, Appl. Optics **30**, 2778 (1991).

[49] N. Majid, S. Dabral, and J. F. McDonald, J. Electron. Mater. **18**, 301 (1989); estimation for root-mean-square diffusion use values for Parylene-N of $\kappa = 0.12\,\mathrm{W/(mK)}$, $\rho = 1.1\,\mathrm{g/cm^3}$, $c_v = 1300\,\mathrm{J/(kgK)}$.

[50] J. E. Hatch, ed., *Aluminum: Properties and Physical Metallurgy* (ASM, Ohio, 1984).

[51] J. B. Fortin and T. Lu, *Chemical Vapor Deposition Polymerization—The Growth and Properties of Parylene Thin Films* (Springer Science, New York, 2004); see Table 6.4 (p. 81).

[52] T. J. Awe, Ph.D. dissertation. University of Nevada, Reno 2009; see p. 204 for expansion data; see Figs. VI.12 and VI.13 for instability amplitudes.

[53] ROI are 512 pixels in axial extent and 95 pixels (57 μm) in azimuth (representing the average strata width). Four nonoverlapping ROI were preselected, with left edges separated by 120 μm. First, Fourier amplitudes $|Y(k)|/n$, where $Y(k) = \sum_{j=1}^{n} (j) e^{-2\pi i (j-1)(k-1)/n}$ and $n = 512$, are calculated for each ROI. Then, for each Fourier mode, a linear fit is found to the natural logarithm of its amplitude from 6 ICCD images at their midframe time, each with 4 ROI (24 amplitudes total), with the slope representing the exponential growth coefficient of that mode. Error bars on individual growth rates denote $\pm 1\sigma$ confidence of the slope. This process was repeated for 35 choices of 4, identically sized ROI, yielding averages $\pm 1\sigma$ of $\gamma_{\max} = 0.061 \pm 0.004\,\mathrm{ns^{-1}}$ and $m = 0.36 \pm 0.04\,\mathrm{ns^{-1}}\,\mu\mathrm{m^2\,rad^{-2}}$, nearly identical to those for slopes of the most separated (highly independent) group of 4 ROI, which are shown in Fig. 4.

[54] J. Stephens, A. Neuber, and M. Kristiansen, Phys. Plasmas **19**, 032702 (2012).

[55] M. P. Desjarlais, J. D. Kress, and L. A. Collins, Phys. Rev. E **66**, 025401(R) (2002).

[56] W. Navidi, *Statistics for Engineers & Scientists*, 4th ed. (McGraw Hill, New York, 2015), p. 548.